GEOPHYSICS, VOL. 89, NO. 3 (MAY-JUNE 2024); P. T151–T162, 15 FIGS.
10.1190/GEO2023-0574.1

Pseudo-Helmholtz decomposition for an elastic VTI wavefield based on wavefront phase direction

Gang Yao[1], Xinyu Fang[1], Qingqing Zheng[2], Di Wu[3], and Fenglin Niu[4]

ABSTRACT

P and S waves are coupled when propagating in anisotropic elastic media. The separation of P and S waves helps to study the characteristics of different types of seismic waves as well as mitigating crosstalk artifacts in elastic reverse time migration and elastic full-waveform inversion. At present, the methods of seismic wave mode separation in anisotropic media are mainly built on divergence- and curl-like operations, pseudo-Helmholtz decomposition, and low-rank approximation. We develop a new pseudo-Helmholtz decomposition operator based on eigenform analysis and the wavefront phase direction to decompose vertically transversely isotropic elastic wavefields. The corresponding P-/S-wave decoupling formulas are also derived in detail. Compared with the divergence- and curl-like methods, the new method does not change the phase of P and S waves. Compared with existing pseudo-Helmholtz decomposition methods based on eigenform analysis, our method achieves more accurate wavefield separation than the zero-order pseudo-Helmholtz decomposition operator. Our method requires solving one vector Poisson equation only, resulting in much less computational cost than the existing first-order pseudo-Helmholtz decomposition methods. In addition, the accuracy of our method is analyzed by providing homogeneous media with different parameter settings. Finally, the numerical examples demonstrate that the new pseudo-Helmholtz decomposition method is effective, efficient, and robust against random noise.

INTRODUCTION

P and S waves are coupled in the process of elastic wave propagation. Wave mode separation can distinguish different types of waves in complex media, which is conducive to studying the propagation characteristics of different types of waves. Moreover, wave mode separation is a key step in suppressing crosstalk artifacts in elastic reverse time migration (ERTM) (e.g., Sun et al., 2006; Yan and Sava, 2008; Du et al., 2012; Wang and McMechan, 2015) and elastic full-waveform inversion (e.g., Ren and Liu, 2016; Wang and Cheng, 2017).

In isotropic media, the polarization directions of P and S waves are parallel and perpendicular to the direction of wave propagation, respectively. Therefore, the input wavefield can be decomposed using the divergence and curl operators directly to obtain a scalar P wave and a vector S wave (Dellinger and Etgen, 1990). However, the amplitude and phase of the separated P and S waves are incorrect. To solve this problem, Zhang and McMechan (2010) propose a vector wavefield decomposition method in the wavenumber domain based on Helmholtz decomposition theory, which gives the correct amplitude and phase. They also extend the Helmholtz decomposition theory to vertically transversely isotropic (VTI) media. In contrast, Zhu (2017) also proposes a vector wavefield decomposition method in the spatial domain based on Helmholtz decomposition theory. This method solves a vector Poisson equation with a fast sine transform. The method of Zhu (2017) shares the same fundamental principle as

Manuscript received by the Editor 28 September 2023; revised manuscript received 19 January 2024; published ahead of production 5 March 2024; published online 29 April 2024.
[1]China University of Petroleum (Beijing), National Key Laboratory of Petroleum Resources and Engineering, Beijing, China; China University of Petroleum (Beijing), China Key Lab of Geophysical Exploration of CNPC, Beijing, China; and China University of Petroleum (Beijing), Unconventional Petroleum Research Institute, Beijing, China. E-mail: yaogang@cup.edu.cn (corresponding author); fangxy@student.cup.edu.cn.
[2]China University of Petroleum (Beijing), National Key Laboratory of Petroleum Resources and Engineering, Beijing, China; China University of Petroleum (Beijing), China Key Lab of Geophysical Exploration of CNPC, Beijing, China; and China University of Petroleum (Beijing), College of Science, Department of Mathematics, Beijing, China. E-mail: zhengqq@cup.edu.cn.
[3]China University of Petroleum (Beijing), National Key Laboratory of Petroleum Resources and Engineering, Beijing, China; China University of Petroleum (Beijing), China Key Lab of Geophysical Exploration of CNPC, Beijing, China; and China University of Petroleum (Beijing), College of Geophysics, Beijing, China. E-mail: wudi@cup.edu.cn.
[4]Rice University, Department of Earth, Environmental and Planetary Sciences, Houston, Texas, USA. E-mail: niu@rice.edu.

DOI:10.1190/geo2023-0574.1

the method of Zhang and McMechan (2010), but they are in two different domains. To improve efficiency, Zhao et al. (2018) and Yang et al. (2018) avoid solving the vector Poisson equation by applying a double integral on the source wavelet and a further scaling operation with phase velocities. Inspired by the Zhu (2017) method, Zheng and Yao (2023) propose a wavefield separation method based on the scalar Poisson equation by using the relations among the operations of the gradient, divergence, curl, and external derivative. This method only needs to solve one Poisson equation, which significantly reduces the computational cost compared with the Zhu (2017) method.

In the real world, most of the earth's rocks are anisotropic elastic media. In anisotropic media, P and S waves are neither parallel nor perpendicular to the direction of wave propagation (Tsvankin, 2012). Dellinger and Etgen (1990) present a wavefield separation technique for anisotropic media. They solve the Christoffel equation in the wavenumber domain to obtain the eigenvectors, which indicate the polarization direction of P and S waves for all required wavenumbers. Then, an inverse Fourier transform is applied to form the separation operator in the space domain. However, they only develop this method for homogeneous media. Yan and Sava (2009) propose non-stationary spatial filtering for anisotropic wavefield separation in heterogeneous media. The separation accuracy depends on the length of the local pseudo-derivative operator. The longer the operator is, the higher the accuracy. They present the operator as long as 65. Methods of Dellinger and Etgen (1990) and Yan and Sava (2009) are analog to the divergence and curl operators for the isotropic case. Thus, the phase and amplitude are incorrect.

To obtain the correct amplitude and phase of P and S wavefields, Zhang and McMechan (2010) propose a VTI vector wavefield decomposition method based on the Helmholtz theory and the Christoffel equation in the wavenumber domain. The method was carried out block by block for heterogeneous media. Each block is treated as homogeneous. Cheng and Fomel (2014) use the low-rank approximation to improve the efficiency of separating anisotropic wavefields in the mixed domain, i.e., spatial and wavenumber domains, but it still requires multiple Fourier transforms.

Yang et al. (2019) propose zero- and first-order pseudo-Helmholtz decomposition operators to decompose anisotropic wavefields in the spatial domain based on eigenform analysis, wherein the auxiliary wavefield is obtained by solving the Poisson equation using lower-upper (LU) decomposition. This auxiliary wavefield can also be approximated by applying the first-order Taylor expansion to the reciprocal of the square of the modulus of the pseudo-gradient operator in the mixed domain (Zhang et al., 2022), where one forward fast Fourier transform (FFT) and two inverse FFTs are used for each component at each time step of the 2D case. Zuo et al. (2022) derive the zero-order pseudo-Helmholtz decomposition operator in the 3D case based on eigenform analysis. The zero-order pseudo-Helmholtz decomposition operator can perfectly decompose the P and S waves for an elliptic anisotropic media. However, for non-elliptic anisotropic media, there are noticeable wavefield residuals, especially when $|\varepsilon - \delta|$ is large. Methods based on eigenform analysis solve the Christoffel equation analytically to obtain a mathematical formula for the eigenvectors. In contrast, the separation methods in the previous paragraphs solve the Christoffel equation for the eigenvectors numerically. Therefore, when the model parameter changes, the computation is repeated. One advantage of these numerical methods is that they work for weak and strong anisotropy.

In this paper, we propose a new pseudo-Helmholtz decomposition operator based on the wavefront's phase direction. There are three advantages of the proposed wavefield decomposition method: first, an approximated anisotropic Poisson equation is derived in the space domain by making use of the phase direction. The accuracy of the proposed anisotropic Poisson equation is higher than that of the first-order pseudo-Helmholtz decomposition based on the assumption of $k_x^2 = k_z^2$ (Yang et al., 2019). Second, there are no mixed high-order derivatives in the proposed decomposition operator; therefore, it has less computational cost than the existing first-order pseudo-Helmholtz decomposition operators. Third, we consider using the successive over-relaxation (SOR) method with alternating sweeping orderings to solve the anisotropic Poisson equation. This method is matrix-free and uses an iterative solution, which can save computation and memory costs compared with LU decomposition (Davis and Duff, 1997).

The rest of this paper is structured as follows. First, we conduct a review of the Christoffel equation and pseudo-Helmholtz decomposition, predicated upon an analysis of eigenforms. Subsequently, we introduce a fresh first-order pseudo-Helmholtz decomposition approach that leverages the eigenform analysis and the wavefront's phase direction. To validate the effectiveness of the new method, three numerical examples are presented. We end with some conclusions.

METHODOLOGY

Eigenvalues and vectors of the Christoffel equation

The 2D elastic VTI wave equation is (Aki and Richards, 2002; Tsvankin, 2012)

$$\begin{cases} \rho(\mathbf{x})\frac{\partial^2 u_x(\mathbf{x},t)}{\partial t^2} = c_{11}(\mathbf{x})\frac{\partial^2 u_x(\mathbf{x},t)}{\partial x^2} + c_{55}(\mathbf{x})\frac{\partial^2 u_x(\mathbf{x},t)}{\partial z^2} + (c_{13}(\mathbf{x}) + c_{55}(\mathbf{x}))\frac{\partial^2 u_z(\mathbf{x},t)}{\partial x \partial z} \\ \rho(\mathbf{x})\frac{\partial^2 u_z(\mathbf{x},t)}{\partial t^2} = c_{55}(\mathbf{x})\frac{\partial^2 u_z(\mathbf{x},t)}{\partial x^2} + c_{33}(\mathbf{x})\frac{\partial^2 u_z(\mathbf{x},t)}{\partial z^2} + (c_{13}(\mathbf{x}) + c_{55}(\mathbf{x}))\frac{\partial^2 u_x(\mathbf{x},t)}{\partial x \partial z} \end{cases}, \tag{1}$$

where $u_x(\mathbf{x}, t)$ and $u_z(\mathbf{x}, t)$ denote the horizontal and vertical displacements, respectively; $\mathbf{x}$ represents the Cartesian coordinate; $\rho(\mathbf{x})$ is the density; and $c_{11}(\mathbf{x})$, $c_{13}(\mathbf{x})$, $c_{33}(\mathbf{x})$, and $c_{55}(\mathbf{x})$ denote the elements of the stiffness matrix for elastic VTI media. They can be expressed by the Thomsen (1986) parameters as follows:

$$\begin{aligned} &c_{11} = \rho(1+2\varepsilon)V_{\mathrm{P}}^2, \quad c_{33} = \rho V_{\mathrm{P}}^2, \quad c_{55} = \rho V_{\mathrm{S}}^2, \\ &c_{13} = \rho\sqrt{[(1+2\delta)V_{\mathrm{P}}^2 - V_{\mathrm{S}}^2][V_{\mathrm{P}}^2 - V_{\mathrm{S}}^2]} - \rho V_{\mathrm{S}}^2, \end{aligned} \tag{2}$$

where V_{P} and V_{S} are the P- and S-wave velocities along the symmetrical axes, respectively.

Based on a local homogeneous assumption, Fourier transforms of equation 1 give the following Christoffel equation:

$$\begin{bmatrix} c_{11}k_x^2 + c_{55}k_z^2 - \rho\omega^2 & (c_{13}+c_{55})k_x k_z \\ (c_{13}+c_{55})k_x k_z & c_{55}k_x^2 + c_{33}k_z^2 - \rho\omega^2 \end{bmatrix} \begin{bmatrix} U_x \\ U_z \end{bmatrix} = 0. \tag{3}$$

If denoting

$$\mathbf{A} = \begin{bmatrix} c_{11}k_x^2 + c_{55}k_z^2 & (c_{13}+c_{55})k_x k_z \\ (c_{13}+c_{55})k_x k_z & c_{55}k_x^2 + c_{33}k_z^2 \end{bmatrix}, \tag{4}$$

then $\lambda = \rho\omega^2 = \rho k^2 v^2$ is the eigenvalue of $\mathbf{A}$, where k denotes the wavenumber and v represents the phase velocity. The eigenvalues of $\mathbf{A}$ are

$$\lambda_{1,2} = \rho\frac{[(1+2\varepsilon)V_P^2 + V_S^2]k_x^2 + [V_P^2 + V_S^2]k_z^2}{2} \pm \rho\frac{[(1+2\varepsilon)V_P^2 - V_S^2]k_x^2 + [V_P^2 - V_S^2]k_z^2}{2} \times \sqrt{1 + \frac{8(\delta-\varepsilon)V_P^2(V_P^2 - V_S^2)k_x^2k_z^2}{[((1+2\varepsilon)V_P^2 - V_S^2)k_x^2 + (V_P^2 - V_S^2)k_z^2]^2}}, \quad (5)$$

and the associated eigenvectors are

$$\begin{cases} \mathbf{V}_1 = \begin{bmatrix} k_x \\ \frac{\rho\sqrt{[(1+2\delta)V_P^2 - V_S^2][V_P^2 - V_S^2]}k_x^2k_z}{\lambda_1 - \rho(V_S^2k_x^2 + V_P^2k_z^2)} \end{bmatrix} \\ \mathbf{V}_2 = \begin{bmatrix} \frac{-\rho\sqrt{[(1+2\delta)V_P^2 - V_S^2][V_P^2 - V_S^2]}k_x^2k_z}{\lambda_2 - \rho((1+2\varepsilon)V_P^2k_x^2 + V_S^2k_z^2)} \\ -k_x \end{bmatrix} \end{cases}. \quad (6)$$

The eigenvectors $\mathbf{V}_1$ and $\mathbf{V}_2$ indicate the polarization directions of the P and S waves, respectively (Dellinger and Etgen, 1990). As $\mathbf{V}_1$ and $\mathbf{V}_2$ are perpendicular to each other in anisotropic media, the P and S waves can be separated by projecting the vector wavefield, e.g., displacement and particle velocity, to the eigenvector directions.

Pseudo-Helmholtz decomposition

The anisotropic elastic wavefield $\mathbf{U}$ in the wavenumber domain can be expressed as

$$\mathbf{U} = \mathbf{U}_0^{\mathbf{P}} + \mathbf{U}_0^{\mathbf{S}}, \quad (7)$$

where $\mathbf{U} = (U_x, U_z)$ is the wavefield in the wavenumber domain obtained by applying the Fourier transform to $\mathbf{u} = (u_x, u_z)$. The terms $\mathbf{U}_0^{\mathbf{P}}$ and $\mathbf{U}_0^{\mathbf{S}}$ are the vector P and S wavefields, respectively. Because the pseudo-Helmholtz decomposition gives an approximation of P and S wavefields, $\mathbf{U}^{\mathbf{P}}$ and $\mathbf{U}^{\mathbf{S}}$ denote the approximate P and S wavefields produced by the pseudo-Helmholtz decomposition in the rest of the paper.

By applying the first-order Taylor expansion on equation 5 (details are shown in Appendix A), the eigenvector $\mathbf{V}_1$ becomes $\mathbf{D}_1$, which is

$$\mathbf{D}_1 = \begin{bmatrix} k_x \\ rk_z \end{bmatrix}, \quad (8)$$

with

$$r = \frac{r_2}{r_1 + \frac{r_4k_z^2}{r_1k_x^2 + r_3k_z^2}}, \quad r_1 = (1+2\varepsilon)V_P^2 - V_S^2, \quad r_2 = \sqrt{[(1+2\delta)V_P^2 - V_S^2][V_P^2 - V_S^2]}, \quad r_3 = V_P^2 - V_S^2, \quad r_4 = 2(\delta-\varepsilon)V_P^2(V_P^2 - V_S^2). \quad (9)$$

By projecting the anisotropic elastic wavefield $\mathbf{U}$ onto the direction $\mathbf{D}_1$, we obtain

$$\begin{cases} \mathbf{D}_1 \cdot \mathbf{U} = \mathbf{D}_1 \cdot \mathbf{U}^{\mathbf{P}} \\ \mathbf{D}_1 \times \mathbf{U}^{\mathbf{P}} = 0 \end{cases} \quad (10)$$

and

$$\begin{cases} \mathbf{D}_1 \times \mathbf{U} = \mathbf{D}_1 \times \mathbf{U}^{\mathbf{S}} \\ \mathbf{D}_1 \cdot \mathbf{U}^{\mathbf{S}} = 0 \end{cases}. \quad (11)$$

According to equations 10 and 11, the pure P wave and pure S wave can be separated using the formula (the details are shown in Appendix B):

$$\begin{cases} \mathbf{U}^{\mathbf{P}} = \mathbf{D}_1\left(\mathbf{D}_1 \cdot \frac{\mathbf{U}}{|\mathbf{D}_1|^2}\right) \\ \mathbf{U}^{\mathbf{S}} = -\mathbf{D}_1 \times \left(\mathbf{D}_1 \times \frac{\mathbf{U}}{|\mathbf{D}_1|^2}\right) \end{cases}. \quad (12)$$

Then, adding $i = \sqrt{-1}$ to equation 12 gives

$$\begin{cases} \mathbf{U}^{\mathbf{P}} = i\mathbf{D}_1(i\mathbf{D}_1 \cdot \mathbf{W}_1) \\ \mathbf{U}^{\mathbf{S}} = -i\mathbf{D}_1 \times (i\mathbf{D}_1 \times \mathbf{W}_1) \\ \mathbf{W}_1 = -\frac{\mathbf{U}}{|\mathbf{D}_1|^2} \end{cases}. \quad (13)$$

Equation 13 is transformed into the spatial domain as follows:

$$\begin{cases} \mathbf{u}^{\mathbf{P}} = \bar{\nabla}(\bar{\nabla} \cdot \mathbf{w}_1) \\ \mathbf{u}^{\mathbf{S}} = -\bar{\nabla} \times (\bar{\nabla} \times \mathbf{w}_1) \end{cases}, \quad (14)$$

where the operator $\bar{\nabla}$ is

$$\bar{\nabla} = \begin{bmatrix} \partial_x \\ r(\mathbf{x})\partial_z \end{bmatrix}, \quad (15)$$

with

$$r(\mathbf{x}) = \frac{r_2(\mathbf{x})}{r_1(\mathbf{x}) + \frac{r_4(\mathbf{x})\partial_z^2}{r_1(\mathbf{x})\partial_x^2 + r_3(\mathbf{x})\partial_z^2}}, \quad r_1(\mathbf{x}) = (1+2\varepsilon(\mathbf{x}))V_P^2(\mathbf{x}) - V_S^2(\mathbf{x}), \quad r_2(\mathbf{x}) = \sqrt{[(1+2\delta(\mathbf{x}))V_P^2(\mathbf{x}) - V_S^2(\mathbf{x})][V_P^2(\mathbf{x}) - V_S^2(\mathbf{x})]}, \quad r_3(\mathbf{x}) = V_P^2(\mathbf{x}) - V_S^2(\mathbf{x}), \quad r_4(\mathbf{x}) = 2(\delta(\mathbf{x}) - \varepsilon(\mathbf{x}))V_P^2(\mathbf{x})(V_P^2(\mathbf{x}) - V_S^2(\mathbf{x})), \quad (16)$$

where ∂_x and ∂_z represent the first-order spatial derivatives along the x- and z-directions, respectively, and $\mathbf{w}_1$ is the auxiliary wavefield that satisfies

$$[\partial_x^2 + r^2(\mathbf{x})\partial_z^2]\mathbf{w}_1(\mathbf{x}) = \mathbf{u}(\mathbf{x}). \quad (17)$$

Equations 14–17 constitute the first-order pseudo-Helmholtz decomposition formulas. By assuming $\delta = \varepsilon$, then $r_4 = 0$, the first-order pseudo-Helmholtz decomposition is reduced to the zero-order pseudo-Helmholtz decomposition. A similar 3D zero-order pseudo-Helmholtz decomposition method has been proposed by Zuo et al. (2022). By assuming $\delta = \varepsilon = 0$, the first-order pseudo-Helmholtz decomposition is further reduced to the Helmholtz decomposition in isotropic media.

DOI:10.1190/geo2023-0574.1

First-order pseudo-Helmholtz decomposition with wavefront's phase direction

The operator, $r_1(\mathbf{x}) + ((r_4(\mathbf{x})\partial_z^2)/(r_1(\mathbf{x})\partial_x^2 + r_3(\mathbf{x})\partial_z^2))$, acts in the denominator in equation 17, which leads to implementation difficulty and extra high costs. Yang et al. (2019) solve the Poisson equation 17 approximately by assuming $k_x = k_z$. To more accurately solve the Poisson equation 17, we present a new pseudo-Helmholtz decomposition operator based on the phase direction of the wavefront.

In the wavenumber domain, the wavenumber vector $\mathbf{k} = (k_x, k_z)$ indicates the phase direction of the corresponding plane wave. The unit vector of the phase direction $\mathbf{n}$ can be computed by

$$\mathbf{n} = (n_x, n_z) = \frac{\mathbf{k}}{|\mathbf{k}|}. \tag{18}$$

Then, the operator $\mathbf{D}_1$ turns into

$$\mathbf{D} = \begin{bmatrix} k_x \\ r' k_z \end{bmatrix}, \tag{19}$$

with

$$r' = \frac{r_2}{r_1 + \frac{r_4 n_z^2}{r_1 n_x^2 + r_3 n_z^2}}. \tag{20}$$

Replacing the operator $\mathbf{D}_1$ in equations 10–13 with $\mathbf{D}$, then transforming them to the spatial domain, gives

$$\begin{cases} \mathbf{u^P} = \nabla'(\nabla' \cdot \mathbf{w}) \\ \mathbf{u^S} = -\nabla' \times (\nabla' \times \mathbf{w}) \end{cases}, \tag{21}$$

where the new pseudo-Helmholtz decomposition operator ∇' is

$$\nabla' = \begin{bmatrix} \partial_x \\ r'(\mathbf{x})\partial_z \end{bmatrix}, \tag{22}$$

$$r'(\mathbf{x}) = \frac{r_2(\mathbf{x})}{r_1(\mathbf{x}) + \frac{r_4(\mathbf{x}) n_z^2}{r_1(\mathbf{x}) n_x^2 + r_3(\mathbf{x}) n_z^2}}, \tag{23}$$

and $\mathbf{w}$ satisfies the following anisotropic Poisson equation:

$$\frac{\partial^2 \mathbf{w}(x,z)}{\partial x^2} + (r'(\mathbf{x}))^2 \frac{\partial^2 \mathbf{w}(x,z)}{\partial z^2} = \mathbf{u}(x,z). \tag{24}$$

Appendix C gives the corresponding derivation and formulas for 3D anisotropic elastic media.

In the spatial domain, the phase direction vector $\mathbf{n}$ can be replaced by using the local phase direction:

$$\mathbf{n} = (n_x, n_z) = \frac{\nabla \mathbf{u}}{|\nabla \mathbf{u}|}. \tag{25}$$

This approach to computing the phase direction can also be seen in Xu and Zhou (2014) for tilted transversely isotropic acoustic wavefield modeling. A more accurate way to compute the local phase direction is the optical flow (Horn and Schunck, 1981; Barron and Thacker, 2005; Xie et al., 2022). Where multiple events cross over each other, the computed wavefront phase direction is an average direction, which is inaccurate for each individual event. However, the wavefront phase direction in this paper is mainly used for the higher-order term in the denominator of equation 23. Therefore, even if the higher-order term contains some errors, it has an insignificant impact on the result at the location of the wave crossing. Moreover, the wavefield decomposition is mainly applied in the ERTM, which uses smooth velocity models, and thus, the wave crossings are reduced greatly.

Equations 21–25 form a new first-order pseudo-Helmholtz wavefield decomposition method. Its main cost is to solve the anisotropic Poisson equation 24. This anisotropic Poisson equation can be solved effectively by using SOR iteration with alternating sweeping orderings (Kincaid and Young, 1972; Zhao, 2005). Here, the second-order derivative is calculated using the sixth-order central finite difference.

Denoting

$$\begin{cases} a(\mathbf{x}) = 1 \\ b(\mathbf{x}) = (r'(\mathbf{x}))^2 \end{cases}, \tag{26}$$

the SOR iteration formula for equation 24 is as follows:

$$w_{i,j}^{(k+1)} = \beta \frac{u_{i,j} - \frac{a_{i,j}}{\Delta x^2}\sum_{n=1}^{3} c_n (w_{i+n,j}^{(k)} + w_{i-n,j}^{(k+1)}) - \frac{b_{i,j}}{\Delta z^2}\sum_{n=1}^{3} c_n (w_{i,j+n}^{(k)} + w_{i,j-n}^{(k+1)})}{c_0 \left(\frac{a_{i,j}}{\Delta x^2} + \frac{b_{i,j}}{\Delta z^2}\right)} + (1-\beta) w_{i,j}^{(k)}, \tag{27}$$

where $u_{i,j}$ is the input wavefield, $w_{i,j}^{(k)}$ represents the value of the kth iteration at position (i,j), c_n represents the finite-difference coefficients, and β is the relaxation factor. The SOR convergence criterion is $\beta \in (0, 2)$. Here, β is generally evaluated by trial and error according to numerical effectiveness. In this paper, experimental examples use $\beta = 1.9$. To accelerate the convergence, SOR iteration with alternating sweeping orderings sweeps the entire region in the following four orders:

$$\begin{aligned} &\text{(i) } i = 1{:}\mathrm{I},\ j = 1{:}\mathrm{J}, \quad \text{(ii) } i = \mathrm{I}{:}1,\ j = 1{:}\mathrm{J}, \\ &\text{(iii) } i = \mathrm{I}{:}1,\ j = \mathrm{J}{:}1, \quad \text{(iv) } i = 1{:}\mathrm{I},\ j = \mathrm{J}{:}1. \end{aligned} \tag{28}$$

SOR starts with the sweeping ordering of (i) in the first iteration and then changes to subsequent sweeping orderings in the next three iterations. After every four iterations, SOR restarts the sweeping orderings. The solution obtained from the previous sweeping ordering is taken as the initial value of the next sweeping ordering. The anisotropic Poisson equation 24 is then solved. There is no need to build a large sparse matrix, which can save the computation costs effectively. More details related to SOR iteration and alternating sweeping orderings can be found in Kincaid and Young (1972) and Zhao (2005).

EXAMPLES

In this section, three numerical experiments are presented to show the effectiveness of the proposed first-order pseudo-Helmholtz decomposition for VTI wavefield separation. The anisotropic Poisson equation 24 is solved by using SOR iteration with alternating sweeping orderings.

VTI layered model

In the first example, the density of the layered model is $\rho = 1000\ \mathrm{kg/m^3}$, and other parameters are shown in Figure 1. The model is discretized using a 1000 × 300 grid with a grid spacing of 10 m. A P-wave source is excited at (distance = 5 km, depth = 0.5 km) using a 15 Hz Ricker wavelet.

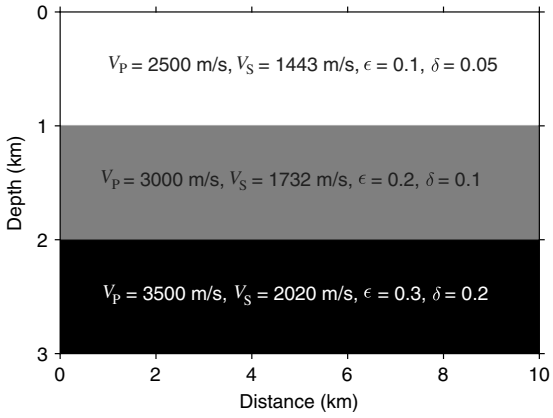

Figure 1. The VTI layered model with its parameters.

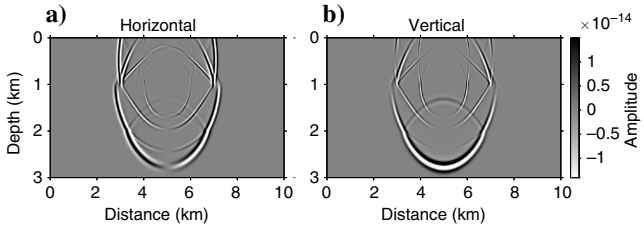

Figure 2. (a) The horizontal and (b) vertical components of the particle velocity wavefields in the VTI layered model at a propagation time of 0.85 s.

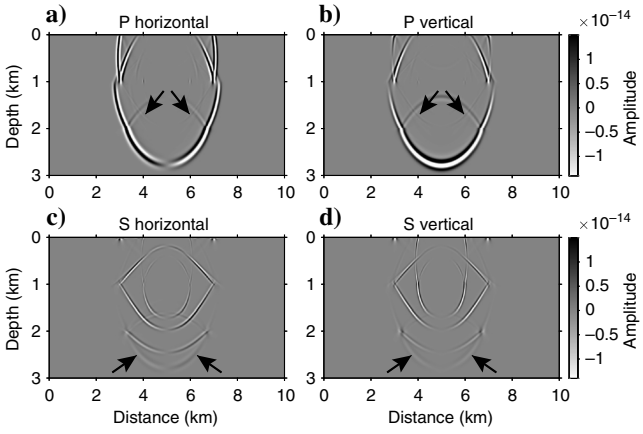

Figure 3. The horizontal and vertical components of the P/S waves in the VTI layered model separated by using the zero-order pseudo-Helmholtz decomposition operator. (a and b) The horizontal and vertical components of the P waves, respectively. (c and d) The counterparts of (a and b) for the S waves, respectively. The black arrows indicate the wave leakages.

The particle velocity wavefields are shown in Figure 2. Figures 3 and 4 depict the P/S waves obtained using the zero-order pseudo-Helmholtz decomposition method presented by Yang et al. (2019) and the first-order pseudo-Helmholtz decomposition method based on the wavefront phase proposed in this paper, respectively. From Figure 3, it can be observed that the P waves obtained using the zero-order pseudo-Helmholtz decomposition method contain residual S waves, and similarly, the S waves also contain residual P waves (as indicated by the black arrows). In contrast, Figure 4 shows that the proposed first-order method has almost no residual wavefield at the same location. Therefore, the proposed method is effective for nonelliptical anisotropic layered models.

Hess model

In the second example, the Hess model is applied to show the effectiveness of the new pseudo-Helmholtz decomposition method. The model parameters of the Hess model are shown in Figure 5. The

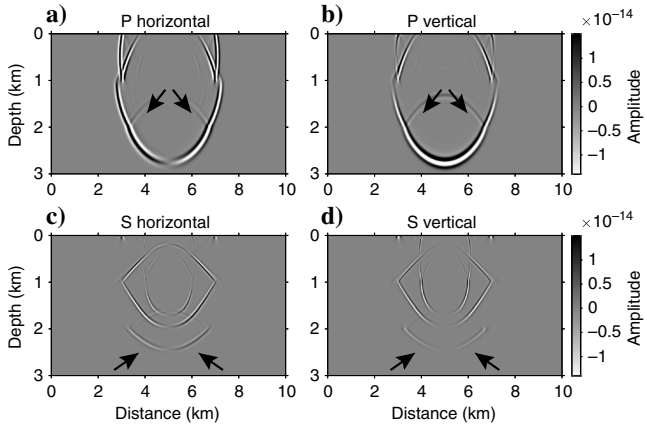

Figure 4. The horizontal and vertical components of the P/Swaves in the VTI layered model separated by using the new first-order pseudo-Helmholtz decomposition operator. (a and b) The horizontal and vertical components of the P waves, respectively. (c and d) The counterparts of (a and b) for the S waves, respectively. The black arrows correspond to those in Figure 3.

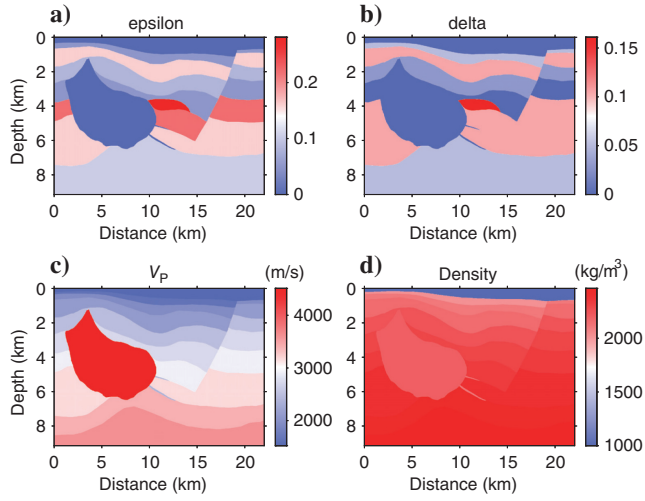

Figure 5. (a–d) The parameters of the Hess model.

S-wave velocity is the P-wave velocity divided by $\sqrt{3}$. A P-wave source with a 5 Hz Ricker wavelet is positioned in the center of the surface. The horizontal and vertical components of the VTI wavefield are shown in Figure 6.

Figures 7 and 8 show the horizontal and vertical components of the separated P/S waves obtained using the zero-order pseudo-Helmholtz decomposition method and the new first-order pseudo-Helmholtz decomposition method, respectively. As shown in Figures 7a, 7b, 8a, and 8b, both methods separate the P wave effectively. However, the wiggle display in Figure 9 indicates that the new first-order pseudo-Helmholtz decomposition produces more accurate amplitudes than the zero-order pseudo-Helmholtz decomposition.

The decomposed S-wave results are shown in Figures 7c, 7d, 8c, and 8d. As can be seen, the zero-order pseudo-Helmholtz decomposition method produces discernible P-wave residuals in the S wave, as indicated by the arrows. In contrast, the energy leakage is reduced significantly in Figure 8c and 8d, thanks to the new first-order pseudo-Helmholtz decomposition method.

Marmousi model

In addition to the Hess model, another general model, Marmousi, is provided here to demonstrate the effectiveness of the method described in this paper. The size and parameters of the Marmousi model are shown in Figure 10. In this model, the S-wave velocity is set as $V_S = V_P/\sqrt{3}$. The grid size of the discrete model is 10 m, and the time interval is 1 ms. A 15 Hz Ricker wavelet is used to excite a P-wave source at the middle of the surface. The previous examples have proven that the new method is better than the zero-order pseudo-Helmholtz decomposition method, which shares the same limitation as observed in the Marmousi model. To avoid repetition, this example only displays the decomposition results of the new method.

Figure 11a and 11b shows the particle velocity wavefields of the horizontal and vertical components, respectively. Figure 11c–11f shows the P/S waves of the horizontal and vertical components obtained by using the new method. This method can decompose the P/S waves well. Figure 11g and 11h shows the wavefield residuals by subtracting the decomposed P and S waves from the original wavefields. The error is about two orders of magnitude smaller than

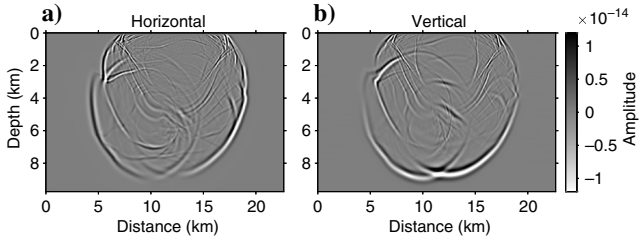

Figure 6. (a) The horizontal and (b) vertical components of the VTI wavefields from the Hess model at a propagation time of 3.6 s.

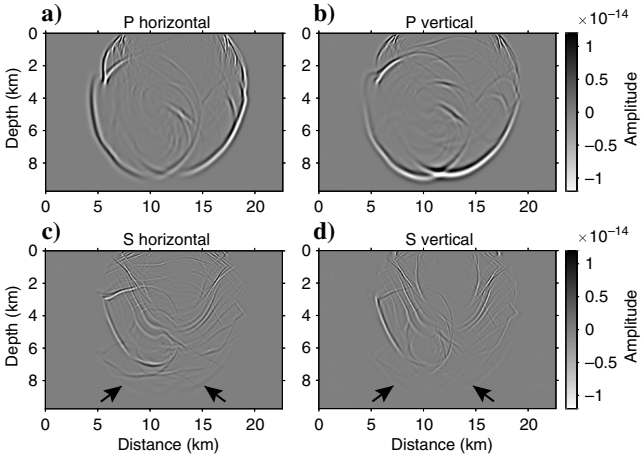

Figure 7. (a) The horizontal and (b) vertical components of the separated P wavefield. (c) The horizontal and (d) vertical components of the separated S wavefield obtained using the zero-order pseudo-Helmholtz decomposition method. The black arrows point to the leaked P-wave energy.

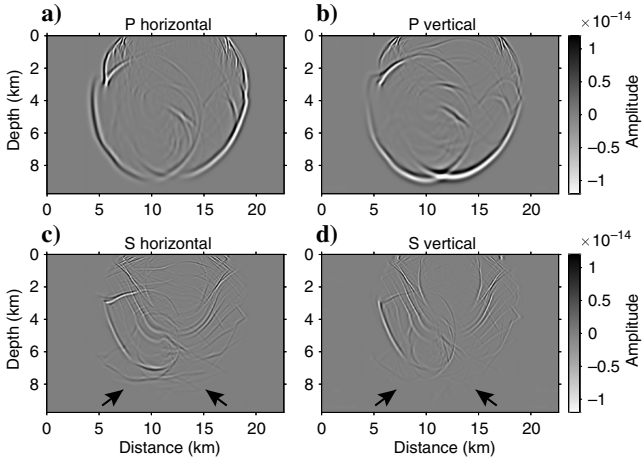

Figure 8. (a) The horizontal and (b) vertical components of the separated P wavefield. (c) The horizontal and (d) vertical components of the separated S wavefield obtained using the new pseudo-Helmholtz decomposition method. The black arrows correspond to those in Figure 7. We see very little leaking P waves at the location indicated by the arrows.

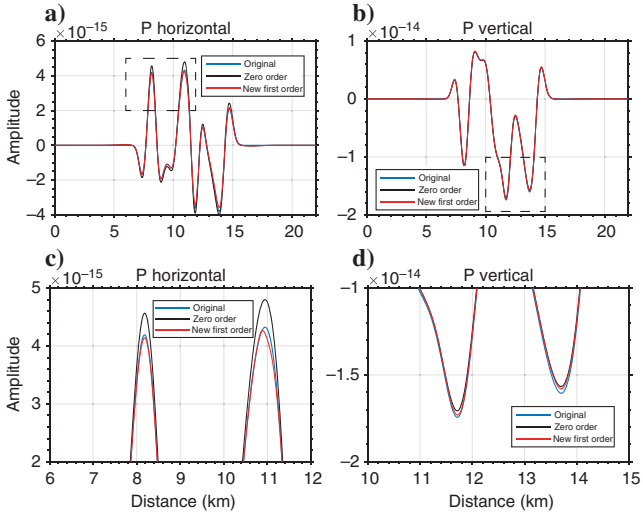

Figure 9. Wiggle display of the (a) horizontal and (b) vertical components of the P waves at a depth of 8.6 km using the zero-order and new pseudo-Helmholtz decomposition methods, respectively. (c and d) Enlarged views of the dashed boxes in (a and b), respectively.

the original wavefield. Therefore, the new method not only decomposes the anisotropic wavefield effectively but also reconstructs it with high accuracy.

In summary, three examples demonstrate that the new first-order pseudo-Helmholtz decomposition method can achieve a clean P-/S-wave decomposition for elastic VTI wavefields and is also suitable for complex VTI models.

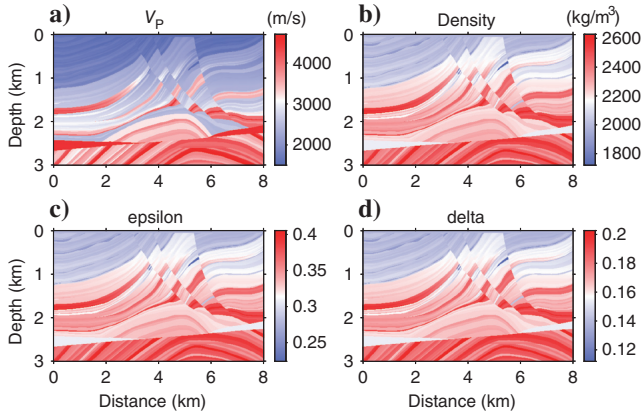

Figure 10. (a–d) The parameters of the Marmousi model.

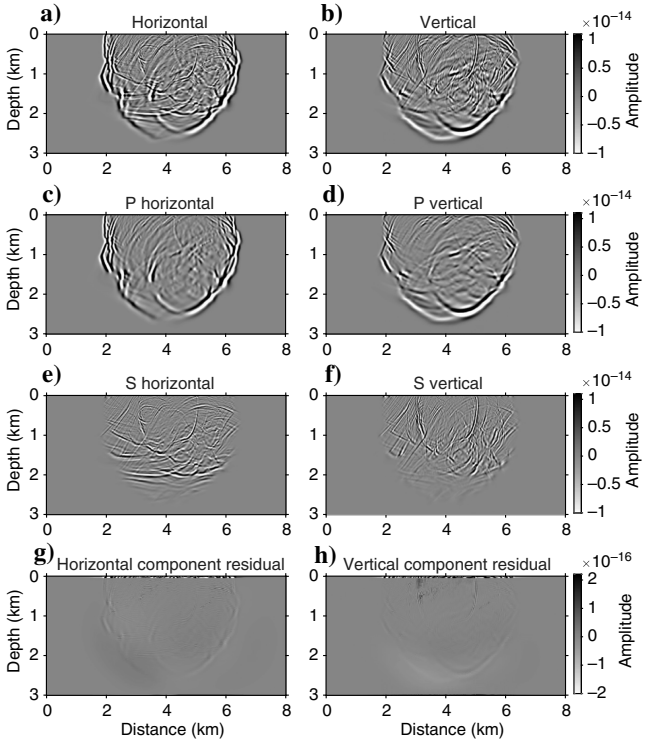

Figure 11. The P-/S-wave separation for the Marmousi model. (a) The horizontal and (b) vertical components of the particle velocity wavefields at a propagation time of 1.1 s. (c and d) The horizontal and vertical components of the P waves, respectively. (e and f) The counterparts of (c and d) for the S waves, respectively. (g and h) The horizontal and vertical components of the wavefield residuals obtained by subtracting the input wavefield from the separated P and S waves, respectively. The residual wavefields are two orders of magnitude smaller than the original wavefields.

DISCUSSION

Precision analysis of wavefield decomposition

The three previous examples have demonstrated that the new first-order pseudo-Helmholtz decomposition method is effective and efficient. Here, we carry out a quantitative precision analysis by varying the anisotropic parameter difference, i.e., $\varepsilon - \delta$, and the V_P/V_S ratio for a set of homogeneous models. The method of Zhang and McMechan (2010), which is accurate for homogeneous models, is used to compute the reference results.

The homogeneous models are discretized into a 600×600 grid with a spacing of 10 m. A vertical force source of a 15 Hz Riker wavelet is excited in the center of the model. The wavefield snapshot at 0.6 s was used to analyze the wavefield decomposition accuracy.

Figure 12a shows how the relative errors of P/S waves change with $\varepsilon - \delta$. The model parameters are $V_P/V_S = \sqrt{3}$, $V_P = 3000$ m/s, $V_S = 1732$ m/s, $\rho = 1000$ kg/m^3, $\delta = 0.1$, $\varepsilon \in [0.1, 0.4]$, and $\varepsilon - \delta \in [0, 0.3]$. The accuracy of this method decreases as the value of $\varepsilon - \delta$ increases. The error is less than 0.5%, when $\varepsilon - \delta = 0.05$, which is a commonly encountered weakly anisotropic medium in practice. Even for a very strong anisotropic medium, $\varepsilon - \delta = 0.3$, the error is less than 6%.

Figure 12b shows how the relative errors of P/S waves change with the ratio of V_P/V_S. The model parameters are $V_P = 3000$ m/s, $\rho = 1000$ kg/m^3, $\varepsilon = 0.3$, $\delta = 0.1$, $V_S \in [1500, 2500]$, and $V_P/V_S \in [1.2, 2]$. As shown in Figure 12b, the accuracy decreases first and then increases as the ratio of V_P/V_S increases. Note that the test models, i.e., $\varepsilon = 0.3$, $\delta = 0.1$, are strongly anisotropic. The errors are much smaller for the commonly encountered weakly anisotropic media. Furthermore, the anisotropy parameter difference, i.e., $\varepsilon - \delta$, has a greater effect on the decomposition accuracy than the V_P/V_S ratio.

Strongly anisotropic media

The proposed first-order pseudo-Helmholtz decomposition method is derived by taking the first-order Taylor expansion on the eigenvalue of the Christoffel equation around $\varepsilon - \delta$. The high-order terms are discarded, resulting in errors when $\varepsilon \neq \delta$. The larger the $\varepsilon - \delta$, the greater the error. Previous examples and quantitative analyses demonstrate that the new method is quite accurate for a commonly encountered weakly anisotropic medium, e.g., $\varepsilon - \delta = 0.05$, and sufficiently accurate for a moderately strong anisotropic medium,

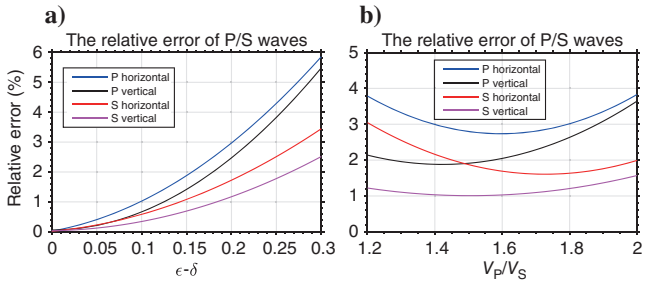

Figure 12. The relative error of the P/S waves obtained by the new method. The method of Zhang and McMechan (2010), which is accurate for homogeneous models, is used to compute the reference results. (a) The relative errors as a function of the difference in anisotropic parameters, i.e., $\varepsilon - \delta$. (b) The relative errors as a function of the V_P/V_S ratio.

e.g., the first-layered model, which has $\varepsilon = 0.3$ and $\delta = 0.2$. To further understand the limits of the new method, we modified the anisotropic parameters of the layered model of the first example into $\varepsilon = 0.25$, 0.3, and 0.4 and $\delta = 0.05$, 0.1, and 0.15, which is strongly anisotropic, i.e., $|\varepsilon - \delta| \geq 0.2$ (Thomsen, 1986). Figure 13 shows the decomposed results. As expected, there are some leaks in the P and S waves, but they are insignificant. The residuals plotted in Figure 13g and 13h are two orders of magnitude smaller than the original wavefields. Figure 14 shows one trace of the separated P/S waves and original wavefields at a distance of 7 km. As can be seen, although there are some amplitude differences and leakages in certain locations, overall, this method has good adaptability to strongly anisotropic media. Thus, this example further demonstrates that the new method is robust and should be sufficient for imaging and inversion.

Effects of noise in P-/S-wave decomposition

To illustrate the effectiveness of the new first-order pseudo-Helmholtz decomposition in resisting noise, Gaussian noise is added to the input wavefields of the Marmousi example. The noise-contaminated wavefields have a signal-to-noise ratio of 1.6 for the horizontal component and 1 for the vertical component, as shown in Figure 15a and 15b. The separated P and S waves are shown in Figure 15c–15f. Compared with the noise-free results in Figure 11, we conclude that the new method is quite effective in resisting noise.

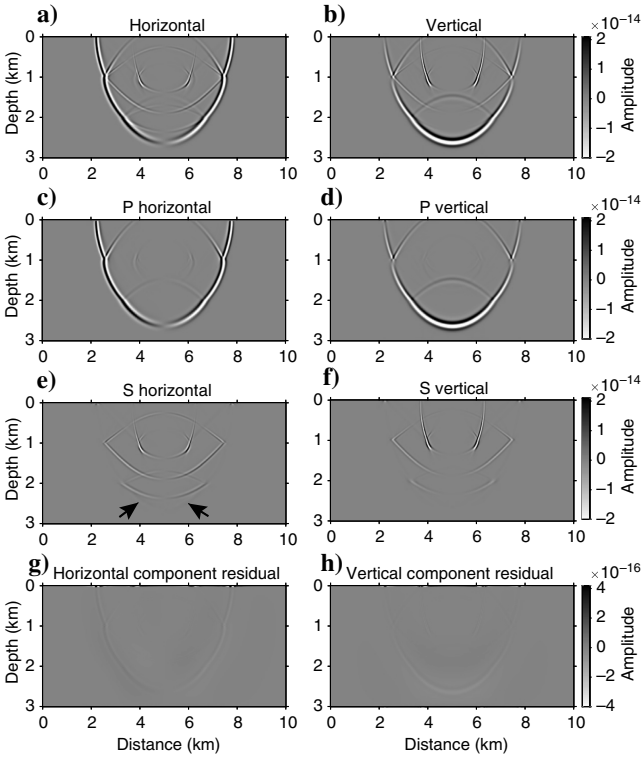

Figure 13. (a) The horizontal and (b) vertical components of particle velocity wavefields in the strongly anisotropic layered model at a propagation time of 1 s. (c and d) The horizontal and vertical components of the P waves, respectively. (e and f) The counterparts of (c and d) for the S waves, respectively. The black arrows indicate the noticeable P-wave leakage. (g and h) The horizontal and vertical components of the wavefield residuals obtained by subtracting the input wavefield from the separated P and S waves, respectively. The residual wavefields are two orders of magnitude smaller than the original wavefields.

Computational efficiency analysis

The main computational cost of the proposed method lies in solving the Poisson equation 24. There are two Poisson equations for 2D wavefields and three Poisson equations for 3D wavefields. The computational complexity of SOR in equation 27 is $\alpha \cdot nt \cdot nx \cdot nz$. Here, nx and nz are the dimensions of the wavefield and nt is the number of iterations. Based on our tests, 20 iterations are sufficient for the simple models, such as the homogeneous models and layered models, and 60 iterations are sufficient for the complex models, e.g., the Marmousi model. The scalar α depends on the finite-difference order, and it is 28 for the six-order finite difference. The proposed method has a computational cost similar to that of the zero-order pseudo-Helmholtz decomposition method by Yang et al. (2019). However, their first-order method solves six Poisson equations for the 2D wavefields. The low-rank method proposed by Cheng and Fomel (2014) includes a one-time forward Fourier transform and r times inverse Fourier transforms, resulting in a computational complexity of $c \cdot (r+1) \cdot nx \cdot nz \cdot \log(nx \cdot nz)$. Here, the value of c depends

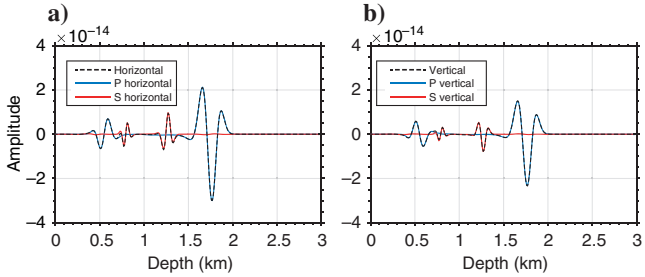

Figure 14. Wiggle display of the (a) horizontal and (b) vertical components of the P and S waves at a distance of 7 km, respectively.

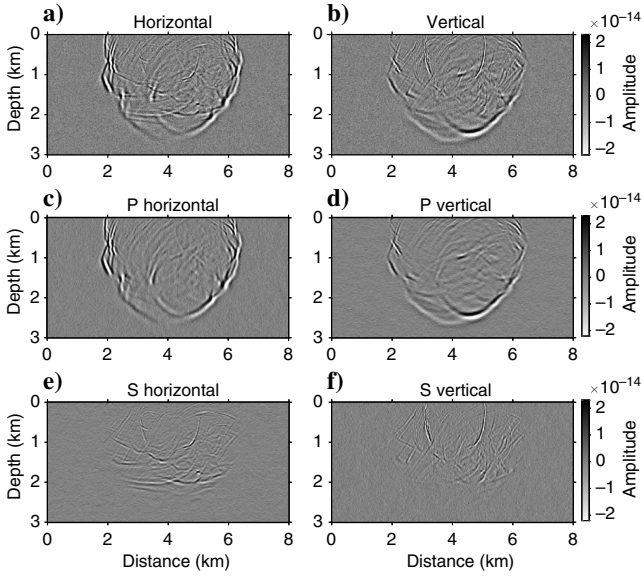

Figure 15. The P-/S-wave separation for the Gaussian noise-contaminated wavefields from the Marmousi model. (a) The horizontal and (b) vertical components of the particle velocity wavefields at a propagation time of 1.1 s. (c and d) The horizontal and vertical components of the P waves, respectively. (e and f) The counterparts of (c and d) for the S waves, respectively.

on the specific implementation and hardware; typically, this is eight (Golub and Van Loan, 2013) and r denotes the reduced rank. Cheng and Fomel (2014) choose $r = 6$ for the Hess VTI model. The low-rank method also involves the cost of matrix decomposition, which is one to two orders of magnitude higher than Fourier transforms (refer to Tables 1 and 2 in Cheng and Fomel, 2014). To mitigate this cost, they propose precomputing the matrices. Therefore, the proposed pseudo-Helmholtz method achieves a similar level of computational efficiency as the low-rank method when the matrix decomposition is not taken into account.

CONCLUSION

In this paper, we propose a new pseudo-Helmholtz decomposition method based on the wavefront's phase direction for elastic VTI wavefields. It overcomes the difficulty of implementing the first-order pseudo-Helmholtz decomposition and its associated anisotropic Poisson equation. SOR iteration with alternating sweeping orderings is used to solve the Poisson equation iteratively. It is more efficient than the LU decomposition methods. Compared with the first-order Helmholtz decomposition method, the new pseudo-Helmholtz decomposition method requires much less computational cost, and more importantly, it is easier to implement the new method in the space domain. Compared with the zero-order pseudo-Helmholtz decomposition method, the new pseudo-Helmholtz decomposition method can obtain more accurate P-/S-wave decomposition at a similar computational cost. Although the first-order Taylor approximation is applied in the new pseudo-Helmholtz decomposition method, accuracy analysis and numerical experiments demonstrate that the accuracy is sufficient for normal elastic VTI models.

ACKNOWLEDGMENTS

This work was supported by the R&D Department of China National Petroleum Corporation (Investigations on fundamental experiments and advanced theoretical methods in geophysical prospecting application, grant nos. 2022DQ0604-02 and 2022DQ0604-03) and the National Nature Science Foundation of China (grant nos. U23B20159 and 42074129). The authors thank Editor-in-Chief A. Malcolm, associate editor, assistant editor, and three reviewers for their constructive and thoughtful comments and suggestions, which have improved the quality of this paper significantly.

DATA AND MATERIALS AVAILABILITY

Data associated with this research are available and can be obtained by contacting the corresponding author. None of the authors have a conflict of interest to disclose.

APPENDIX A

DERIVATION OF THE EIGENVALUES AND VECTORS OF THE CHRISTOFFEL EQUATION

Based on the Christoffel equation 3, we denote

$$\mathbf{A} = \begin{bmatrix} c_{11}k_x^2 + c_{55}k_z^2 & (c_{13}+c_{55})k_xk_z \\ (c_{13}+c_{55})k_xk_z & c_{55}k_x^2 + c_{33}k_z^2 \end{bmatrix} \tag{A-1}$$

and

$$\mathbf{V} = \begin{bmatrix} V_1 \\ V_2 \end{bmatrix}. \tag{A-2}$$

Then, $\lambda = \rho\omega^2 = \rho k^2 v^2$ (v is the phase velocity) and $\mathbf{V}$ are the eigenvalue and eigenvector of the matrix $\mathbf{A}$, respectively. According to the eigen analysis theory, we form the following determinant:

$$|\mathbf{A} - \lambda\mathbf{E}| = \begin{vmatrix} c_{11}k_x^2 + c_{55}k_z^2 - \lambda & (c_{13}+c_{55})k_xk_z \\ (c_{13}+c_{55})k_xk_z & c_{55}k_x^2 + c_{33}k_z^2 - \lambda \end{vmatrix} = 0. \tag{A-3}$$

From equation A-3, we obtain a quadratic equation for the variable λ:

$$a\lambda^2 + b\lambda + c = 0, \tag{A-4}$$

where

$$\begin{cases} a = 1 \\ b = -[(c_{11}k_x^2 + c_{55}k_z^2) + (c_{55}k_x^2 + c_{33}k_z^2)] \\ c = (c_{11}k_x^2 + c_{55}k_z^2)\cdot(c_{55}k_x^2 + c_{33}k_z^2) - (c_{13}+c_{55})^2k_x^2k_z^2 \end{cases}. \tag{A-5}$$

Then, λ in equation A-4 can be solved by

$$\begin{aligned} \lambda_{1,2} &= \frac{-b \pm \sqrt{b^2 - 4ac}}{2a} \\ &= \frac{(c_{11}+c_{55})k_x^2 + (c_{33}+c_{55})k_z^2}{2} \\ &\pm \frac{[(c_{11}-c_{55})k_x^2 + (c_{33}-c_{55})k_z^2]}{2} \\ &\times \sqrt{1 + \frac{4[(c_{11}-c_{55})\cdot(c_{55}-c_{33}) + (c_{13}+c_{55})^2]k_x^2k_z^2}{[(c_{11}-c_{55})k_x^2 + (c_{33}-c_{55})k_z^2]^2}}. \end{aligned} \tag{A-6}$$

Note c_{11}, c_{13}, c_{33}, and c_{55} can be replaced with the Thomsen parameters given in equation 2. Therefore,

$$\begin{aligned} \lambda_{1,2} &= \rho\frac{[(1+2\varepsilon)V_P^2 + V_S^2]k_x^2 + [V_P^2 + V_S^2]k_z^2}{2} \\ &\pm \rho\frac{[(1+2\varepsilon)V_P^2 - V_S^2]k_x^2 + [V_P^2 - V_S^2]k_z^2}{2} \\ &\times \sqrt{1 + \frac{8(\delta-\varepsilon)V_P^2(V_P^2 - V_S^2)k_x^2k_z^2}{[((1+2\varepsilon)V_P^2 - V_S^2)k_x^2 + (V_P^2 - V_S^2)k_z^2]^2}}. \end{aligned} \tag{A-7}$$

Let $\mathbf{V}_1 = \begin{bmatrix} x_1 \\ x_2 \end{bmatrix}$. Then, we obtain

$$\begin{cases} (c_{11}k_x^2 + c_{55}k_z^2)x_1 + (c_{13}+c_{55})k_xk_zx_2 = \lambda x_1 \\ (c_{13}+c_{55})k_xk_zx_1 + (c_{55}k_x^2 + c_{33}k_z^2)x_2 = \lambda x_2 \end{cases}. \tag{A-8}$$

Assuming $x_1 = k_x$, the second equation in equation A-8 gives

$$x_2 = \frac{(c_{13}+c_{55})k_x^2k_z}{\lambda_1 - (c_{55}k_x^2 + c_{33}k_z^2)}. \tag{A-9}$$

Therefore, the eigenvector associated with λ_1 can be written as

$$\mathbf{V}_1 = \begin{bmatrix} k_x \\ \frac{(c_{13}+c_{55})k_x^2 k_z}{\lambda_1-(c_{55}k_x^2+c_{33}k_z^2)} \end{bmatrix} = \begin{bmatrix} k_x \\ \frac{\rho\sqrt{[(1+2\delta)V_P^2-V_S^2][V_P^2-V_S^2]}k_x^2 k_z}{\lambda_1-\rho(V_S^2k_x^2+V_P^2k_z^2)} \end{bmatrix}. \tag{A-10}$$

Similarly, assuming $x_2 = -k_x$, the first equation in equation A-8 gives

$$x_1 = \frac{-(c_{13}+c_{55})k_x^2 k_z}{\lambda_2-(c_{11}k_x^2+c_{55}k_z^2)}. \tag{A-11}$$

Therefore, the eigenvector corresponding to λ_2 can be written as

$$\mathbf{V}_2 = \begin{bmatrix} \frac{-(c_{13}+c_{55})k_x^2 k_z}{\lambda_2-(c_{11}k_x^2+c_{55}k_z^2)} \\ -k_x \end{bmatrix} = \begin{bmatrix} \frac{-\rho\sqrt{[(1+2\delta)V_P^2-V_S^2][V_P^2-V_S^2]}k_x^2 k_z}{\lambda_2-\rho((1+2\varepsilon)V_P^2k_x^2+V_S^2k_z^2)} \\ -k_x \end{bmatrix}. \tag{A-12}$$

For the nonelliptic anisotropy problem ($\varepsilon \neq \delta$), when $\varepsilon - \delta \to 0$, the eigenvalues can be obtained by the first-order Taylor expansion of the radical term of equation A-7:

$$\begin{cases} \lambda_1 = \rho V_P^2[(1+2\varepsilon)k_x^2+k_z^2] + \rho\frac{2(\delta-\varepsilon)V_P^2(V_P^2-V_S^2)k_x^2k_z^2}{[(1+2\varepsilon)V_P^2-V_S^2]k_x^2+(V_P^2-V_S^2)k_z^2} \\ \lambda_2 = \rho V_S^2[k_x^2+k_z^2] - \rho\frac{2(\delta-\varepsilon)V_P^2(V_P^2-V_S^2)k_x^2k_z^2}{[(1+2\varepsilon)V_P^2-V_S^2]k_x^2+(V_P^2-V_S^2)k_z^2} \end{cases}. \tag{A-13}$$

Then, the eigenvectors of $\mathbf{A}$ can be obtained by substituting equation A-13 into equation A-10 and equation A-12:

$$\begin{cases} \mathbf{V}_1 = \begin{bmatrix} k_x \\ \frac{\sqrt{[(1+2\delta)V_P^2-V_S^2][V_P^2-V_S^2]}}{[(1+2\varepsilon)V_P^2-V_S^2]+\frac{2(\delta-\varepsilon)V_P^2(V_P^2-V_S^2)k_z^2}{[(1+2\varepsilon)V_P^2-V_S^2]k_x^2+(V_P^2-V_S^2)k_z^2}}k_z \end{bmatrix} \\ \mathbf{V}_2 = \begin{bmatrix} \frac{\sqrt{[(1+2\delta)V_P^2-V_S^2][V_P^2-V_S^2]}}{[(1+2\varepsilon)V_P^2-V_S^2]+\frac{2(\delta-\varepsilon)V_P^2(V_P^2-V_S^2)k_z^2}{[(1+2\varepsilon)V_P^2-V_S^2]k_x^2+(V_P^2-V_S^2)k_z^2}}k_z \\ -k_x \end{bmatrix} \end{cases}. \tag{A-14}$$

Physically, λ_1 and λ_2 represent the phase velocities of the P and S waves, respectively. In addition, $\mathbf{V}_1$ and $\mathbf{V}_2$ denote the polarization directions of the P and S waves, respectively. Based on equation A-14, the eigenvectors of the matrix $\mathbf{A}$ can also be expressed as follows:

$$\begin{cases} \mathbf{V}_1 = \begin{bmatrix} k_x \\ \frac{\sqrt{[(1+2\delta)V_P^2-V_S^2][V_P^2-V_S^2]}}{[(1+2\varepsilon)V_P^2-V_S^2]+\frac{2(\delta-\varepsilon)V_P^2(V_P^2-V_S^2)k_z^2}{[(1+2\varepsilon)V_P^2-V_S^2]k_x^2+(V_P^2-V_S^2)k_z^2}}k_z \end{bmatrix} = \begin{bmatrix} k_x \\ rk_z \end{bmatrix} \\ \mathbf{V}_2 = \begin{bmatrix} \frac{\sqrt{[(1+2\delta)V_P^2-V_S^2][V_P^2-V_S^2]}}{[(1+2\varepsilon)V_P^2-V_S^2]+\frac{2(\delta-\varepsilon)V_P^2(V_P^2-V_S^2)k_z^2}{[(1+2\varepsilon)V_P^2-V_S^2]k_x^2+(V_P^2-V_S^2)k_z^2}}k_z \\ -k_x \end{bmatrix} = \begin{bmatrix} rk_z \\ -k_x \end{bmatrix} \end{cases}, \tag{A-15}$$

where

$$r = \frac{r_2}{r_1+\frac{r_4k_z^2}{r_1k_x^2+r_3k_z^2}}, \tag{A-16}$$

where r_1, r_2, r_3, and r_4 are the functions given in equation 9.

Because the elliptic anisotropy problem ($\varepsilon = \delta$) is a special case of the non-elliptic anisotropy problem, its eigenvalues and eigenvectors of $\mathbf{A}$ can be obtained in equations A-13 and A-15:

$$\begin{cases} \lambda_1 = \rho V_P^2[(1+2\varepsilon)k_x^2+k_z^2] \\ \lambda_2 = \rho V_S^2[k_x^2+k_z^2] \end{cases} \tag{A-17}$$

and

$$\begin{cases} \mathbf{V}_1 = \begin{bmatrix} k_x \\ \frac{r_2}{r_1}k_z \end{bmatrix} \\ \mathbf{V}_2 = \begin{bmatrix} \frac{r_2}{r_1}k_z \\ -k_x \end{bmatrix} \end{cases}. \tag{A-18}$$

APPENDIX B

DERIVATION OF THE FIRST-ORDER PSEUDO-HELMHOLTZ DECOMPOSITION

According to Helmholtz's theorem, the vector anisotropic elastic wavefield $\mathbf{u}$ can be resolved into the sum of a curl-free vector field and a divergence-free vector field:

$$\mathbf{u} = \mathbf{u_0^P} + \mathbf{u_0^S}, \tag{B-1}$$

where $\mathbf{u_0^P}$ and $\mathbf{u_0^S}$ are the P and S wavefields, respectively. Applying the Fourier transform to $\mathbf{u} = (u_x, u_z)$ gives $\mathbf{U} = (U_x, U_z)$ in the wavenumber domain. The terms $\mathbf{U_0^P}$ and $\mathbf{U_0^S}$ are the vector P and S wavefields in the wavenumber domain, respectively, satisfying

$$\begin{cases} \mathbf{V}_1 \cdot \mathbf{U} = \mathbf{V}_1 \cdot \mathbf{U_0^P} \\ \mathbf{V}_1 \times \mathbf{U_0^P} = 0 \end{cases} \tag{B-2}$$

and

$$\begin{cases} \mathbf{V}_1 \times \mathbf{U} = \mathbf{V}_1 \times \mathbf{U_0^S} \\ \mathbf{V}_1 \cdot \mathbf{U_0^S} = 0 \end{cases}. \tag{B-3}$$

By applying the first-order Taylor expansion in equation 5, the eigenvector $\mathbf{V}_1$ becomes $\mathbf{D}_1$. Then, equations B-2 and B-3 become

$$\begin{cases} \mathbf{D}_1 \cdot \mathbf{U} = \mathbf{D}_1 \cdot \mathbf{U^P} \\ \mathbf{D}_1 \times \mathbf{U^P} = 0 \end{cases} \tag{B-4}$$

and

$$\begin{cases} \mathbf{D}_1 \times \mathbf{U} = \mathbf{D}_1 \times \mathbf{U^S} \\ \mathbf{D}_1 \cdot \mathbf{U^S} = 0 \end{cases}. \tag{B-5}$$

Here,

$$\begin{cases} \mathbf{D}_1 = \begin{bmatrix} k_x \\ rk_z \end{bmatrix} \\ r = \dfrac{r_2}{r_1 + \frac{r_4 k_z^2}{r_1 k_x^2 + r_3 k_z^2}} \end{cases}. \tag{B-6}$$

Based on equation B-4, we can obtain

$$\begin{cases} k_x U_x + rk_z U_z = k_x U_x^p + rk_z U_z^p \\ rk_z U_x^p - k_x U_z^p = 0 \end{cases}. \tag{B-7}$$

Hence

$$\begin{cases} U_x^p = (k_x^2 U_x + rk_x k_z U_z)/(k_x^2 + r^2 k_z^2) \\ U_z^p = (rk_x k_z U_x + r^2 k_z^2 U_z)/(k_x^2 + r^2 k_z^2) \end{cases}. \tag{B-8}$$

Moreover, from equation B-5, we obtain

$$\begin{cases} rk_z U_x - k_x U_z = rk_z U_x^s - k_x U_z^s \\ k_x U_x^s + rk_z U_z^s = 0 \end{cases}. \tag{B-9}$$

Thus, we have

$$\begin{cases} U_x^s = (r^2 k_z^2 U_x - rk_x k_z U_z)/(k_x^2 + r^2 k_z^2) \\ U_z^s = (k_x^2 U_z - rk_x k_z U_x)/(k_x^2 + r^2 k_z^2) \end{cases}. \tag{B-10}$$

Formula B-1 can also be written as

$$\begin{cases} U_x = U_x^p + U_x^s \\ U_z = U_z^p + U_z^s \end{cases}. \tag{B-11}$$

Combining this formula with equations B-8, B-10, and B-11, we have

$$\begin{cases} U_x = (k_x^2 U_x + r^2 k_z^2 U_x)/(k_x^2 + r^2 k_z^2) \\ U_z = (k_x^2 U_z + r^2 k_z^2 U_z)/(k_x^2 + r^2 k_z^2) \end{cases}. \tag{B-12}$$

Formulas B-8, B-10, and B-12 can also be expressed as follows:

$$\begin{cases} \mathbf{U^P} = \mathbf{D}_1 \left(\mathbf{D}_1 \cdot \frac{\mathbf{U}}{|\mathbf{D}_1|^2} \right) \\ \mathbf{U^S} = -\mathbf{D}_1 \times \left(\mathbf{D}_1 \times \frac{\mathbf{U}}{|\mathbf{D}_1|^2} \right) \\ [k_x^2 + r^2 k_z^2] \frac{\mathbf{U}}{|\mathbf{D}_1|^2} = \mathbf{U} \end{cases}. \tag{B-13}$$

After adding $i = \sqrt{-1}$ to equation B-13, we obtain

$$\begin{cases} \mathbf{U^P} = i\mathbf{D}_1 (i\mathbf{D}_1 \cdot \mathbf{W}) \\ \mathbf{U^S} = -i\mathbf{D}_1 \times (i\mathbf{D}_1 \times \mathbf{W}) \\ \mathbf{W} = -\frac{\mathbf{U}}{|\mathbf{D}_1|^2} \\ -[k_x^2 + r^2 k_z^2]\mathbf{W} = \mathbf{U} \end{cases}. \tag{B-14}$$

APPENDIX C

NEW FIRST-ORDER PSEUDO-HELMHOLTZ DECOMPOSITION FOR 3D WAVEFIELDS

For 3D VTI media, the matrix A in equation A-1 turns into

$$\mathbf{A} = \begin{bmatrix} c_{11}k_x^2 + c_{66}k_y^2 + c_{44}k_z^2 & (c_{11} - c_{66})k_x k_y & (c_{13} + c_{44})k_x k_z \\ (c_{11} - c_{66})k_x k_y & c_{66}k_x^2 + c_{11}k_y^2 + c_{44}k_z^2 & (c_{13} + c_{44})k_y k_z \\ (c_{13} + c_{44})k_x k_z & (c_{13} + c_{44})k_y k_z & c_{44}k_x^2 + c_{44}k_y^2 + c_{33}k_z^2 \end{bmatrix}. \tag{C-1}$$

Then, the eigenvalues of matrix $\mathbf{A}$ can be obtained as follows:

$$\begin{aligned} \lambda_{1,3} &= \rho \frac{[(1+2\varepsilon)V_P^2 + V_S^2](k_x^2 + k_y^2) + [V_P^2 + V_S^2]k_z^2}{2} \\ &\pm \rho \frac{[(1+2\varepsilon)V_P^2 - V_S^2](k_x^2 + k_y^2) + [V_P^2 - V_S^2]k_z^2}{2} \\ &\times \sqrt{1 + \frac{8(\delta - \varepsilon)V_P^2(V_P^2 - V_S^2)(k_x^2 + k_y^2)k_z^2}{[((1+2\varepsilon)V_P^2 - V_S^2)(k_x^2 + k_y^2) + (V_P^2 - V_S^2)k_z^2]^2}}, \\ \lambda_2 &= \rho V_S^2[(1+2\gamma)(k_x^2 + k_y^2) + k_z^2]. \end{aligned} \tag{C-2}$$

For the non-elliptic anisotropy problem ($\varepsilon \neq \delta$), the eigenvalues can be obtained by the first-order Taylor expansion of the square-root term of equation C-2:

$$\begin{cases} \lambda_1 = \rho V_P^2[(1+2\varepsilon)(k_x^2 + k_y^2) + k_z^2] + \rho \frac{2(\delta-\varepsilon)V_P^2(V_P^2 - V_S^2)(k_x^2 + k_y^2)k_z^2}{((1+2\varepsilon)V_P^2 - V_S^2)(k_x^2 + k_y^2) + (V_P^2 - V_S^2)k_z^2} \\ \lambda_2 = \rho V_S^2[(1+2\gamma)(k_x^2 + k_y^2) + k_z^2] \\ \lambda_3 = \rho V_S^2[k_x^2 + k_y^2 + k_z^2] - \rho \frac{2(\delta-\varepsilon)V_P^2(V_P^2 - V_S^2)(k_x^2 + k_y^2)k_z^2}{((1+2\varepsilon)V_P^2 - V_S^2)(k_x^2 + k_y^2) + (V_P^2 - V_S^2)k_z^2} \end{cases}, \tag{C-3}$$

where λ_1, λ_2, and λ_3 represent the phase velocities of the P, SH, and SV waves, respectively.

The Christoffel equation for 3D VTI media is

$$\begin{cases} [c_{11}k_x^2 + c_{66}k_y^2 + c_{44}k_z^2]x_1 + [(c_{11} - c_{66})k_x k_y]x_2 + [(c_{13} + c_{44})k_x k_z]x_3 = \lambda x_1 \\ [(c_{11} - c_{66})k_x k_y]x_1 + [c_{66}k_x^2 + c_{11}k_y^2 + c_{44}k_z^2]x_2 + [(c_{13} + c_{44})k_y k_z]x_3 = \lambda x_2 \\ [(c_{13} + c_{44})k_x k_z]x_1 + [(c_{13} + c_{44})k_y k_z]x_2 + [c_{44}k_x^2 + c_{44}k_y^2 + c_{33}k_z^2]x_3 = \lambda x_3 \end{cases}. \tag{C-4}$$

Similar to the 2D case, the eigenvectors for 3D problems can also be obtained by the Christoffel equation C-4 using the first-order Taylor expansion method. Let the eigenvectors correspond to λ_1, λ_2, and λ_3 be $\mathbf{V}_1$, $\mathbf{V}_2$, and $\mathbf{V}_3$, respectively. Then,

$$\begin{cases} \mathbf{V}_1 = \begin{bmatrix} k_x \\ k_y \\ rk_z \end{bmatrix} \\ \mathbf{V}_2 = \begin{bmatrix} -k_y \\ k_x \\ 0 \end{bmatrix} \\ \mathbf{V}_3 = \begin{bmatrix} -rk_x k_z \\ -rk_y k_z \\ k_x^2 + k_y^2 \end{bmatrix} \end{cases}, \tag{C-5}$$

with

$$r = \frac{r_2}{r_1 + \frac{r_4 k_z^2}{r_1(k_x^2+k_y^2)+r_3 k_z^2}}. \tag{C-6}$$

Physically, $\mathbf{V}_1$, $\mathbf{V}_2$, and $\mathbf{V}_3$ are the polarization directions of the P, SH, and SV waves, respectively. Thus, we define the operator $\mathbf{D}_1$ as follows:

$$\mathbf{D}_1 = \begin{bmatrix} k_x \\ k_y \\ rk_z \end{bmatrix}. \tag{C-7}$$

In the wavenumber domain, the wavenumber vector $\mathbf{k} = (k_x, k_y, k_z)$ indicates the phase direction of the corresponding plane wave. Let the unit vector of the phase direction be $\mathbf{n}$. Then, it can be expressed by

$$\mathbf{n} = (n_x, n_y, n_z) = \frac{\mathbf{k}}{|\mathbf{k}|}. \tag{C-8}$$

Then, the operator $\mathbf{D}_1$ turns to

$$\mathbf{D} = \begin{bmatrix} k_x \\ k_y \\ r'k_z \end{bmatrix}, \tag{C-9}$$

where

$$r' = \frac{r_2}{r_1 + \frac{r_4 n_z^2}{r_1(n_x^2+n_y^2)+r_3 n_z^2}}. \tag{C-10}$$

Similar to replacing the operator $\mathbf{D}_1$ in equations 10–13 with $\mathbf{D}$, and then transforming them to the spatial domain, we have

$$\begin{cases} \mathbf{u^P} = \nabla'(\nabla' \cdot \mathbf{w}) \\ \mathbf{u^S} = -\nabla' \times (\nabla' \times \mathbf{w}) \end{cases}, \tag{C-11}$$

where the new pseudo-Helmholtz decomposition operator ∇' is

$$\nabla' = \begin{bmatrix} \partial_x \\ \partial_y \\ r'(\mathbf{x})\partial_z \end{bmatrix}, \tag{C-12}$$

where

$$r'(\mathbf{x}) = \frac{r_2(\mathbf{x})}{r_1(\mathbf{x}) + \frac{r_4(\mathbf{x}) n_z^2}{r_1(\mathbf{x})(n_x^2+n_y^2)+r_3(\mathbf{x}) n_z^2}}, \tag{C-13}$$

and $\mathbf{w}$ satisfies the following anisotropic Poisson equation:

$$\left(\frac{\partial}{\partial x^2} + \frac{\partial}{\partial y^2} + (r'(\mathbf{x}))^2 \frac{\partial}{\partial z^2}\right)\mathbf{w} = \mathbf{u}. \tag{C-14}$$

REFERENCES

Aki, K., and P. Richards, 2002, Quantitative seismology, 2nd ed.: University Science Books.

Barron, J., and N. Thacker, 2005, Tutorial: Computing 2D and 3D optical flow, https://www.researchgate.net/publication/250873492_Tutorial_Computing_2D_and_3D_Optical_Flow, 28 September 2023.

Cheng, J., and S. Fomel, 2014, Fast algorithms for elastic-wave-mode separation and vector decomposition using low-rank approximation for anisotropic media: Geophysics, **79**, no. 4, C97–C110, doi: 10.1190/geo2014-0032.1.

Davis, T., and I. Duff, 1997, An unsymmetric-pattern multifrontal method for sparse LU factorization: SIAM Journal on Matrix Analysis and Applications, **18**, 140–158, doi: 10.1137/S0895479894246905.

Dellinger, J., and J. Etgen, 1990, Wave-field separation in two-dimensional anisotropic media: Geophysics, **55**, 914–919, doi: 10.1190/1.1442906.

Du, Q., Y. Zhu, and J. Ba, 2012, Polarity reversal correction for elastic reverse time migration: Geophysics, **77**, no. 2, S31–S41, doi: 10.1190/geo2011-0348.1.

Golub, G. H., and C. F. Van Loan, 2013, Matrix computations, 4th ed.: Johns Hopkins University Press.

Horn, B. K. P., and B. G. Schunck, 1981, Determining optical flow: Artificial Intelligence, **17**, 185–203, doi: 10.1016/0004-3702(81)90024-2.

Kincaid, D., and D. Young, 1972, The modified successive overrelaxation method with fixed parameters: Mathematics of Computation, **26**, 705–717, doi: 10.1090/S0025-5718-1972-0331746-2.

Ren, Z., and Y. Liu, 2016, A hierarchical elastic full-waveform inversion scheme based on wavefield separation and the multistep-length approach elastic full-waveform inversion: Geophysics, **81**, no. 3, R99–R123, doi: 10.1190/geo2015-0431.1.

Sun, R., G. McMechan, C. S. Lee, J. Chow, and C. H. Chen, 2006, Prestack scalar reverse-time depth migration of 3D elastic seismic data: Geophysics, **71**, no. 5, S199–S207, doi: 10.1190/1.2227519.

Thomsen, L., 1986, Weak elastic anisotropy: Geophysics, **51**, 1954–1966, doi: 10.1190/1.1442051.

Tsvankin, I., 2012, Seismic signatures and analysis of reflection data in anisotropic media, 3rd ed.: SEG.

Wang, T., and J. Cheng, 2017, Elastic full waveform inversion based on mode decomposition: The approach and mechanism: Geophysical Journal International, **209**, 606–622, doi: 10.1093/gji/ggx038.

Wang, W., and G. A. McMechan, 2015, Vector-based elastic reverse time migration: Geophysics, **80**, no. 6, S245–S258, doi: 10.1190/geo2014-0620.1.

Xie, C., P. Song, Z. Zou, J. Tan, S. Wang, and B. Zhao, 2022, Cross-correlation weighted reverse time migration with wavefield decomposition based on optical flow vector: Chinese Journal of Geophysics, **65**, 2260–2275, doi: 10.6038/cjg2022P0328.

Xu, S., and H. Zhou, 2014, Accurate simulations of pure quasi-P-waves in complex anisotropic media: Geophysics, **79**, no. 6, T341–T348, doi: 10.1190/geo2014-0242.1.

Yan, J., and P. Sava, 2008, Isotropic angle-domain elastic reverse-time migration: Geophysics, **73**, no. 6, S229–S239, doi: 10.1190/1.2981241.

Yan, J., and P. Sava, 2009, Elastic wave-mode separation for VTI media: Geophysics, **74**, no. 5, WB19–WB32, doi: 10.1190/1.3184014.

Yang, J., H. Zhang, Y. Zhao, and H. Zhu, 2019, Elastic wavefield separation in anisotropic media based on eigenform analysis and its application in reverse-time migration: Geophysical Journal International, **217**, 1290–1313, doi: 10.1093/gji/ggz085.

Yang, J., H. Zhu, W. Wang, Y. Zhao, and H. Zhang, 2018, Isotropic elastic reverse time migration using the phase- and amplitude-corrected vector P- and S-wavefields: Geophysics, **83**, no. 6, S489–S503, doi: 10.1190/geo2018-0023.1.

Zhang, L., L. Liu, F. Niu, J. Zuo, D. Shuai, W. Jia, and Y. Zhao, 2022, A novel and efficient engine for P-/S-wave-mode vector decomposition for vertical transverse isotropic elastic reverse time migration: Geophysics, **87**, no. 4, S185–S207, doi: 10.1190/geo2021-0609.1.

Zhang, Q., and G. A. McMechan, 2010, 2D and 3D elastic wavefield vector decomposition in the wavenumber domain for VTI media: Geophysics, **75**, no. 3, D13–D26, doi: 10.1190/1.3431045.

Zhao, H., 2005, A fast sweeping method for eikonal equations: Mathematics of Computation, **74**, 603–627, doi: 10.1090/S0025-5718-04-01678-3.

Zhao, Y., H. Zhang, J. Yang, and T. Fei, 2018, Reducing artifacts of elastic reverse time migration by the deprimary technique deprimary ERTM: Geophysics, **83**, no. 6, S569–S577, doi: 10.1190/geo2018-0260.1.

Zheng, Q., and G. Yao, 2023, An improved elastic wavefield separation method based on the Helmholtz decomposition: Geophysics, **88**, no. 4, T203–T210, doi: 10.1190/geo2022-0628.1.

Zhu, H., 2017, Elastic wavefield separation based on the Helmholtz decomposition elastic wavefield separation: Geophysics, **82**, no. 2, S173–S183, doi: 10.1190/geo2016-0419.1.

Zuo, J., F. Niu, L. Liu, S. Da, H. Zhang, J. Yang, L. Zhang, and Y. Zhao, 2022, 3D anisotropic P- and S-mode wavefields separation in 3D elastic reverse-time migration: Surveys in Geophysics, **43**, 673–701, doi: 10.1007/s10712-021-09688-8.

Biographies and photographs of the authors are not available.